A high-dimensional, stochastic model for twin-screw granulation
Part 1: Model description

Andrew D. McGuire[a], Sebastian Mosbach[a], Kok Foong Lee[a], Gavin Reynolds[b], Markus Kraft[a,c,*]

[a]*Department of Chemical Engineering and Biotechnology, University of Cambridge, Philippa Fawcett Dr, Cambridge, CB3 0AS, United Kingdom*
[b]*Pharmaceutical Technology & Development, AstraZeneca, Charter Way, Macclesfield, SK10 2NA, United Kingdom*
[c]*School of Chemical and Biomedical Engineering, Nanyang Technological University, 62 Nanyang Drive, Singapore 637459*

Abstract

In this work we present a novel four-dimensional, stochastic population balance model for twin-screw granulation. The model uses a compartmental framework to reflect changes in mechanistic rates between different screw element geometries. This allows us to capture the evolution of the material along the barrel length. The predictive power of the model is assessed across a range of liquid-solid feed ratios through comparison with experimental particle size distributions. The model results show a qualitative agreement with experimental trends and a number of areas for model improvement are discussed. A sensitivity analysis is carried out to assess the effect of key operating variables and model parameters on the simulated product particle size distribution. The stochastic treatment of the model allows the particle description to be readily extended to track more complex particle properties and their transformations.

Keywords: granulation, twin-screw, stochastic, population balance model

*Corresponding author
Email address:* `mk306@cam.ac.uk` (Markus Kraft)

1. Introduction

Granulation (also known as agglomeration, pelletisation or balling) is a common method of particle manufacture. The formation of granules is a key process in the food industry, in formation of tablets within the pharmaceutical industry and in the production of fertilisers [1]. The granular product will have an optimum size (typically a distribution), porosity, solubility, mechanical strength, shape and flow-ability amongst other properties dictated by the specific application. Granules have several advantages over a simple mixture of the raw ingredients such as better flow-ability; better transport properties (such as limited separation of components and reduced risk of powder explosions); dissolution behaviour and controlled release of Active Pharmaceutical Ingredients (API) [2, 3].

Twin-screw granulation (TSG) is a relatively new method of continuous granule production and is currently subject to a high degree of research as a viable alternative to batch granulation. TSG consists of a barrel with two co-rotating screws into which raw excipient/API are fed in conjunction with a liquid binder as illustrated in Figure 1. In these systems, the screws and barrel wall impart a shear force on the material, forming granules which are then conveyed along the barrel towards the outlet, undergoing a number of transformations such as growth/attrition along the way, depending on the processing conditions.
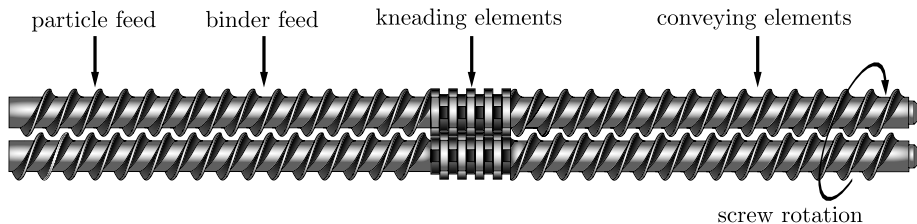

Figure 1: twin-screw granulator

TSG systems have shown many advantages over traditional batch production methods such as the ability to: produce flow-able granules with high API

2

content [4]; reduce plant foot print [5]; minimise the use of API/excipient dur-
ing formulation development and ease the scale-up from development to full
production. [6].

Another advantage of TSG equipment is the variable configuration of the
device available to the operator during formulation development. Each screw
in the TSG system is composed of numerous screw elements which may be of
varying geometry. Different types of element act differently on the particle mass
passing through them and thus the screw element configuration may be altered
to produce a granular product with different physical properties. The screw
speed, liquid feed rate and powder feed formulation may also be varied in this
way, resulting in a system with an exceptionally large operating space. The
complexity and variability of the TSG system therefore requires a deep under-
standing of the underlying process in order to predict, and more importantly,
control the properties of the resulting granules, in line with the philosophy of
Quality by Design [7].

Experimental studies have probed the effects of screw element configuration
on the physical properties of the granular product from TSG systems and tried
to identify the role of specific types of screw element [8, 9, 10, 11]. Dhenge *et.
al.* have investigated the effect of powder feed rate [12] and binder viscosity [13]
while Li et al. [14] and Vanhoorne et al. [15] have assessed the impact of the
physical properties of the API on the TSG process. Hagrasy et al. [16] investi-
gated the effect of powder feed formulation and liquid-solid mass feed ratio on
product size/porosity distribution and Saleh et al. [17] investigated the effect of
binder delivery method on the TSG system. Though the number of experimen-
tal investigations is extensive, the large operating window of TSG systems often
limits the applicability of these results to local regions of the operating space.
The comprehensive review of the experimental TSG literature by Seem et al.
[18] shows a complex interplay between the role of each screw element type,
the overall screw configuration, feed formulation and liquid flowrates on the ob-
served experimental trends. This emphasises the need for a particle-scale model
of TSG that can accurately predict the physical properties of the bulk granular

3

product. Ultimately, the inversion of such a model could then be carried out and coupled with process control systems to allow specification and control of product specification in TSG systems.

Granular systems are generally modelled using population balance models (PBM) [19, 20, 21, 2, 22, 23, 24, 25, 26, 27]. TSG specific PBMs have been developed, ranging from one [28] to three dimensional particle models [29, 30]. A lumped parameter method is typically used to estimate additional particle properties beyond those explicitly tracked by the model [29]. Flow information and collision data have been incorporated into TSG models through couplings with alternative modelling frameworks such as the discrete element method (DEM) [29] and experimental near-infrared chemical tracing [31, 28]. Many of these TSG PBM studies have shown results in qualitative agreement with the experimental studies; however, quantitative predictions have proven to be much more challenging. One reason for this could be over-simplification of the system within the models. All of the existing TSG PBM models are numerically solved using variations of the sectional method [32]. Such a numerical approach ultimately limits the model dimensionality as high dimensional models become computationally unfeasible, thereby placing a limit on model complexity.

The main objective of this work is to extend the stochastic batch granulation model introduced by Braumann et al. [24] and further developed by Lee et al. [33] to twin-screw granulation. Specifically, this involves the introduction/adaption of existing particle process models to reflect differences in the nature of batch and twin-screw processes (such as nucleation dynamics, continuous inflow/outflow) and rectify identified deficiencies in the existing modelling framework. By stochastically evolving the twin-screw particle ensemble in time, the particle representation may be arbitrarily complex. The additional particle dimensions not afforded to traditional sectional methods can then be integrated in the twin-screw process description.

In the first part of this two-part study we present a four-dimensional stochastic population balance model of a TSG system. In the second part of this study we present and analyse the numerical methods developed to overcome the nu-

4

merical challenges inherent to stochastic modelling of twin-screw systems and solve the TSG model described in this paper. The model is used to simulate the experiments carried out by Hagrasy et al. [16], specifically those testing the effect of varying liquid-solid ratio (LSR) using a <u>Lactose Impalpable</u> placebo feed formulation.

The remainder of the paper is structured as follows: firstly we present an overview of the existing population balance model for high shear granulation developed by Braumann et al. [24] and Lee et al. [33]. A detailed account of the twin-screw model mechanisms is given in Section 2.2. The parameter estimation methodology used to evaluate unknown process rate constants is then briefly discussed, followed by a presentation and discussion of the main results in Section 4. Finally, the main findings and future recommendations for TSG modelling are summarised in Section 5.

2. Methodology

2.1. Population balance model

A four-dimensional population balance model is used as the base for the twin-screw granulation model in this study. A general account of the underlying population balance model and the twin-screw specific features are outlined in this section. For a detailed description of the underlying population balance model, the reader is directed to [33, 23].

Building on the work of Lee et al. [33], the granulator is represented by a series of connected, well-mixed <u>compartments</u> filled with particles. In this work we use the type-space $\mathbb{X}$ in which elements $x = (s_{\mathrm{o}}, l_{\mathrm{e}}, l_{\mathrm{i}}, p), x \in \mathbb{X}$ are used to describe each particle. Here: s_{o} is the original solid volume, l_{e} is the external liquid volume, l_{i} is the internal liquid volume and the pore volume as illustrated in Figure 2. Internal liquid only exists within the pore volume and the remaining pore volume is occupied with gas. The same particle vector is capable of representing any of the phases present in a placebo granulation system, namely: primary particles, granules and free liquid droplets.
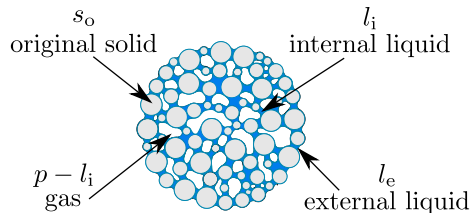
Figure 2: Particle description.

Using this particle description, the total particle volume is:

$$v(x) = s_o(x) + l_e(x) + p(x) \tag{1}$$

and the particle porosity is defined as:

$$\varepsilon(x) = \frac{p(x)}{v(x)}. \tag{2}$$

Particles are assumed to be spherical for the purposes of computing particle surface areas and diameters, however, all non-liquid particles are assumed to have surface asperities with characteristic length scale h_a. These asperities, along with other properties, control the likelihood of successful coalescence between two particles, described further in Section 2.2.

2.2. Twin-screw particle processes

The particles ensemble is evolved in time through a mixture of particle jump events and continuous processes as shown in Figure 3. The possible jump events are: nucleation, particle collision (which may or may not lead to rebound, coalescence and particle compaction), particle breakage and particle transport (between compartments). Liquid penetration (transforming external liquid to internal liquid) is carried out as a continuous particle process. In this work, we make use of the idea of deferred processes as defined by the Linear Process Deferment Algorithm [34]. This algorithm is utilised to defer the applications of linear process operators that are particularly computationally intensive, such as liquid penetration.
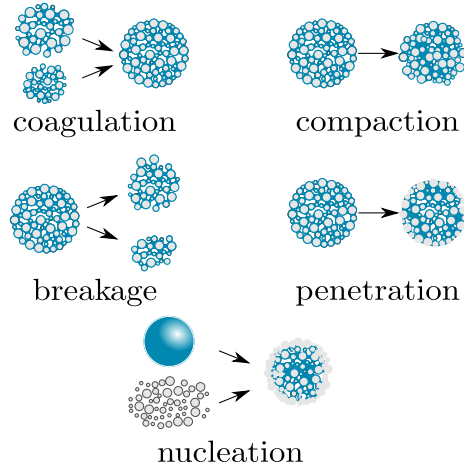
Figure 3: Particle processes permitted in the TSG model.

Since the population balance model is to be solved using the stochastic particle method, it is constructed in weak form. That is to say, each of the terms is integrated against some suitable test function. Let

1. z denote the spatial location of each quantity (i.e. the compartment index).

2. $\lambda(z, t, \mathrm{d}x)$ be a concentration measure on $\mathbb{X}$ at time t in compartment z, or more simply, a concentration measure on the interval $x + \mathrm{d}x$ in compartment z at time, t.

3. Addition and subtraction on $\mathbb{X}$ correspond to particle coagulation and breakage, respectively.

4. $\varphi(z, x) : \mathbb{X} \mapsto \mathbb{R}$ be a suitable test function which is smooth with compact support,

5. $\mathbb{X}_{\mathrm{nuc}} \subset \mathbb{X}$ be the set of all partially formed granular nuclei.

6. $\mathbb{X}_{\mathrm{incept}} \subset \mathbb{X}$ be the set of all possible inception particle forms.

7

The weak form of the population balance equation (PBE) to be solved is then

$$\frac{\mathrm{d}}{\mathrm{d}t} \int_{x \in \mathbb{X}} \varphi(z, x) \lambda(z, t, \mathrm{d}x) = \tag{3}$$

$$\int_{x \in \mathbb{X}_{\mathrm{incept}}} \varphi(z, x) I_{\mathrm{solid}}(z, t, \mathrm{d}x)$$

$$+ \frac{1}{2} \int_{x, y, \xi, \zeta \in \mathbb{X}} [\varphi(z, \xi + \zeta) - \varphi(z, x) - \varphi(z, y)] K_{\mathrm{coag}}(z, \xi, \zeta)$$

$$\mathbb{P}(D_t x = \mathrm{d}\xi) \mathbb{P}(D_t y = \mathrm{d}\zeta)$$

$$\lambda(z, t, \mathrm{d}x) \lambda(z, t, \mathrm{d}y)$$

$$+ \frac{1}{2} \int_{x, y, \xi \in \mathbb{X}} [\varphi(z, \xi) - \varphi(z, \xi - y) - \varphi(z, x)] F(z, \xi, \mathrm{d}y)$$

$$\mathbb{P}(D_t x = \mathrm{d}\xi) \lambda(z, t, \mathrm{d}x)$$

$$+ \int_{x, \xi \in \mathbb{X}} \varphi(z, \xi) \frac{1}{\tau(z - 1)} \mathbb{P}(D_t x = \mathrm{d}\xi) \lambda(z - 1, t, \mathrm{d}x)$$

$$- \int_{x, \xi \in \mathbb{X}} \varphi(z, \xi) \frac{1}{\tau(z)} \mathbb{P}(D_t x = \mathrm{d}\xi) \lambda(z, t, \mathrm{d}x)$$

$$+ \int_{x \in \mathbb{X}} \varphi(z, x) I_{\mathrm{drop}}(z, t, \mathrm{d}x)$$

$$+ \int_{x, \xi \in \mathbb{X}_{\mathrm{nuc}}, y, \zeta \in \mathbb{X} - \mathbb{X}_{\mathrm{nuc}}} [\varphi(z, T_{\mathrm{nuc}}(\xi, \zeta)) - \varphi(z, x) - \varphi(z, y)]$$

$$K_{\mathrm{nuc}}(z, \xi, \zeta) \mathbb{P}(D_t x = \mathrm{d}\xi) \mathbb{P}(D_t y = \mathrm{d}\zeta)$$

$$\lambda(z, t, \mathrm{d}x) \lambda(z, t, \mathrm{d}y).$$

145   In this form, each integral on the RHS of Equation (3) represents an aggregate particle processes within the model. The $\varphi(\cdot)$ component of each integrand represents the particle transformation of the associated mechanism. The remainder of the integrand defines the rate at which this event occurs. The first term in Equation (3) represents the inception of solid particle into the system (simulat-

150   ing the inflow of feed powder). The second term in (3) combines the birth and death terms related to coagulation processes. The third term of Equation (3) represents the birth and death terms associated with particle fragmentation.

The fourth and fifth terms of Equation (3) capture the inter-compartment particle transport processes. The second last term in Equation (3) represents the inception of liquid droplets into the liquid addition zone of the twin-screw. Finally, the last term in Equation (3) concerns the growth of nuclei within the twin-screw device. The physical model and type-space transformations associated with each of these particle processes will be explained, in detail, in the remained of this section.

Liquid addition/nucleation

In TSG, primary agglomerates are generally formed by way of immersion nucleation [13, 35, 36] as small primary particles diffuse into large liquid droplets that are incident on the surface of the powder bed. This mechanism is relevant for TSG, as liquid will typically be added without the use of an atomisation nozzle, and primary particles are typically very small (common commercial lactose excipient blends such GranuLac 200 (Meggle Pharma) have a d50 of around 30μm [37]). It is hypothesised that these liquid-rich primary agglomerates (or nuclei) are subject to compaction and breakage, particularly in kneading elements, as described by the destructive nucleation mechanism of Vonk et al. [38]. Here we adapt an interpretation of the immersion nucleation mechanism to the type-space of the current model.

Liquid addition

The nucleation process begins with the inception of a large droplet. Spherical liquid droplets, consisting only of external liquid and with volume v_{drop} and diameter d_{drop}, are incepted into the first compartment with the form

$$x_{\mathrm{drop}} = (0, v_{\mathrm{drop}}, 0, 0). \tag{4}$$

Droplets are considered to be mono-disperse and d_{drop} is assumed to be the same as the nozzle diameter of the liquid inception port d_{nozzle}. The associated rate of this process (which features in PBE (3)) is

$$I_{\mathrm{drop}}(z, t, \mathrm{d}x) = \frac{(\mathrm{LSR})\dot{M}_{\mathrm{feed}}}{V_{\mathrm{real}}(z)\rho_{\mathrm{l}}v_{\mathrm{drop}}}\delta_{x_{\mathrm{drop}}}(x)\mathrm{d}x. \tag{5}$$

Here $V_{\mathrm{real}}(z)$ is physical volume of the compartment z, $\dot{M}_{\mathrm{feed}}(z)$ is the liquid

9

flow-rate delivered to compartment z, LSR is the liquid-solid mass feed ratio, v_{drop} is the volume of the droplets being incepted and $\delta_{x_{\mathrm{drop}}}$ is to be interpreted as the Dirac delta function, centred on x_{drop}. This results in a total droplet inception rate of

$$R_{\mathrm{drop}}(z,t) = \begin{cases} \dfrac{(\mathrm{LSR})\dot{M}_{\mathrm{feed}}}{v_{\mathrm{drop}}\rho_{\mathrm{l}}}, & \text{if } z = 1, \\ 0, & \text{otherwise,} \end{cases} \tag{6}$$

Nuclei growth

In this work, nuclei growth is defined as the addition of particles to a droplet or semi-formed nuclei (a droplet which has acquired some degree of solid mass) Hence, it is similar to a coagulation event, with the caveat that it involves a droplet/partially formed nucleus and and another particle, which is not a droplet or partially formed nucleus. Further to this, immersion nucleation is defined as the process by which a droplet is incepted into the system, undergoes growth and produces as fully formed nucleus. The nuclei growth is described by the following particle size transformation:

$$x_{\mathrm{nuc}}, x_i \mapsto T_{\mathrm{nuc}}(x_{\mathrm{nuc}}, x_i), \tag{7}$$

where $x_{\mathrm{nuc}} \in \mathbb{X}_{\mathrm{nuc}}, x_i \in \mathbb{X} \setminus \mathbb{X}_{\mathrm{nuc}}$ ($\mathbb{X}_{\mathrm{nuc}}$ is the set of partially formed nuclei).

The nucleation type-space transformation T_{nuc} is characterised by the individual property transformations:

$$s_{\mathrm{o}}(T_{\mathrm{nuc}}(x_{\mathrm{nuc}}, x_i)) = s_{\mathrm{o}}(x_{\mathrm{nuc}}) + s_{\mathrm{o}}(x_i) \tag{8}$$

$$l_{\mathrm{e}}(T_{\mathrm{nuc}}(x_{\mathrm{nuc}}, x_i)) = l_{\mathrm{e}}(x_{\mathrm{nuc}}) \tag{9}$$
$$- \min\left([\phi_{\max} - \phi(x_i)]\mathbb{1}_{\{x|\phi(x_i)\leq\phi_{\max}\}}(x_i)s_{\mathrm{o}}(x_i), l_{\mathrm{e}}(x_{\mathrm{nuc}})\right),$$

$$l_{\mathrm{i}}(T_{\mathrm{nuc}}(x_{\mathrm{nuc}}, x_i)) = l_{\mathrm{i}}(x_{\mathrm{nuc}}) + l_{\mathrm{i}}(x_i) + l_{\mathrm{e}}(x_i) \tag{10}$$
$$+ \min\left([\phi_{\max} - \phi(x_i)]\mathbb{1}_{\{x|\phi(x_i)\leq\phi_{\max}\}}(x_i)s_{\mathrm{o}}(x_i), l_{\mathrm{e}}(x_{\mathrm{nuc}})\right),$$

$$p(T_{\mathrm{nuc}}(x_{\mathrm{nuc}}, x_i)) = l_{\mathrm{i}}(T_{\mathrm{nuc}}(x_{\mathrm{nuc}}, x_i))/s^*. \tag{11}$$

In the above, $\mathbb{1}_{\mathcal{A}}$ is to be interpreted as the indicator function on set $\mathcal{A}$, $\phi(x_i)$

10

is the liquid saturation level of the particle to be added, given as:

$$\phi(x) = \frac{l_{\mathrm{i}}(x) + l_{\mathrm{e}}(x)}{s_{\mathrm{o}}(x)}, \tag{12}$$

and ϕ_{max} is the maximum level of liquid saturation in the nuclei. To quantify this value we follow a similar approach to that taken by Barrasso and Ramachandran [39] to model the size of newly formed nuclei. This approach is consistent with the nucleation mechanism described by Iveson et al. [1], where nuclei are formed by way of droplet penetration into a porous bed. This is captured by the relation:

$$\phi_{\mathrm{max}} = \frac{(1 - \varepsilon_{\mathrm{bed}})s^*}{\varepsilon_{\mathrm{bed}}}, \tag{13}$$

where $\varepsilon_{\mathrm{bed}}$ is the bed packing fraction and s^* is the maximum internal pore liquid saturation level of the nuclei. The probability that a particle will be selected to form part of a nucleus is assumed to be proportional to the volume of the particle. Additionally, it is postulated that there is a maximum particle size that can be integrated into the nucleus. In this study we set the size limit for integration $v_{\mathrm{nuc}}^{\mathrm{max}} = v_{\mathrm{drop}}$. These model properties can be expressed using a nucleation kernel of the form

$$K_{\mathrm{nuc}}(x_{\mathrm{nuc}}, x_i, z, t) = \begin{cases} k_{\mathrm{nuc}}(z) \min(v(x_{\mathrm{nuc}}), v(x_i)) & \text{if } \min(v(x_{\mathrm{nuc}}), v(x_i)) < v_{\mathrm{drop}}, \\ 0 & \text{otherwise}, \end{cases}$$

where k_{nuc} is the nucleation growth rate constant and since, for the conditions we wish to model $v(x_{\mathrm{nuc}}) > v(x_i) \ \forall \ i \in \{1, \ldots, N(z, t)\}$, this can be simplified to

$$K_{\mathrm{nuc}}(x_{\mathrm{nuc}}, x_i, z, t) = \begin{cases} k_{\mathrm{nuc}}(z)v(x_i) & \text{if } v(x_i) < v_{\mathrm{drop}}, \\ 0 & \text{otherwise}. \end{cases} \tag{14}$$

175   As noted by Hapgood et al. [40], with α-Lactose formulations and water binders, the droplet penetration time can likely be considered to be negligible. Hence, it is assumed that particle addition to the nuclei is instantaneous (i.e. $k_{\mathrm{nuc}}(z) \to \infty, \ \forall z$). Given this assumption, at the point of droplet inception,

11

nuclei-growth events occur rapidly (and without intermediate events such as
breakage etc.) on the same partially formed nuclei particle (initially a droplet)
until the product particle $T_{\mathrm{nuc}}(x_{\mathrm{nuc}}, x_i) \notin \mathbb{X}_{\mathrm{nuc}}$. When this condition is met,
i.e the initial droplet has become saturated in with solid, the nuclei growth
process is complete. As such, the droplet inception and sequential nuclei-growth
process can be grouped together into a unified immersion nucleation event. Thus
permitting the formation of large, highly porous, liquid rich agglomerates in the
droplet zone.

Collision/compaction

Model particles may undergo binary collisions according to the transformations

$$\text{Coalescence successful: } (x_i), (x_j) \rightarrow (T_{\mathrm{comp}}(T_{\mathrm{coag}}(x_i, x_j)),$$

$$\text{Coalescence unsuccessful: } (x_i), (x_j) \rightarrow (T_{\mathrm{comp}}(x_i)), (T_{\mathrm{comp}}(x_j)),$$

where T_{comp} and T_{coag} are the compaction and coagulation transforms, respec-
tively.

The rate of collision between particles x_i and x_j is modelled using the size
independent collision kernel:

$$K_{\mathrm{col}}(z, x_i, x_j) = n_{\mathrm{screw}} k_{\mathrm{col}}(z), \tag{15}$$

where n_{screw} is the screw speed and k_{col} is the collision rate constant. Each
particle collision leads to the compaction of the particles involved. This is
modelled as a porosity reduction described by:

$$\Delta\epsilon(x) = \begin{cases} k_{\mathrm{comp}}(z)[\epsilon(x) - \epsilon_{\mathrm{min}}], & \text{if } \epsilon(x) \geq \epsilon_{\mathrm{min}}, \\ 0, & \text{otherwise}, \end{cases} \tag{16}$$

where k_{comp} is the compaction rate constant and ϵ_{min} is the minimum porosity
permitted.

Whether or not a particular collision is successful (resulting in coagulation
of the parent particles) is governed by the Stokes criterion [41]. This criterion
states that, given a collision particle pair (x_i, x_j), coalescence only occurs if

$$\mathrm{St}_{\mathrm{v}}(x_i, x_j) \leq \mathrm{St}_{\mathrm{v}}^*(x_i, x_j), \tag{17}$$

12

where $\mathrm{St_v}$ is the viscous Stokes number and $\mathrm{St_v^*}$ is the critical stokes number.

The viscous Stokes number is defined as [41]

$$\mathrm{St_v}(x_i, x_j) = \frac{\tilde{m}(x_i, x_j)U_{\mathrm{col}}}{3\pi\mu\tilde{R}(x_i, x_j)^2},\tag{18}$$

where $\tilde{m}$ is the mean harmonic mass of the collision pair, U_{col} is the collision velocity, μ is the binder viscosity and $\tilde{R}$ is the harmonic mean radius of the collision pair.

The critical Stokes number is defined as [23]

$$\mathrm{St_v^*}(x_i, x_j) = \left(1 + \frac{1}{e_{\mathrm{coag}}}\right)\ln\left(\frac{\bar{h}_\mathrm{l}(x_i, x_j)}{h_\mathrm{a}}\right),\tag{19}$$

where e_{coag} is the coefficient of restitution of the granule material, $\bar{h}_\mathrm{l}$ is arithmetic average binder thickness of the collision pair and h_a is the height of surface asperities. As in [23], individual particle binder levels h_l are computed as

$$h_\mathrm{l}(x) = \frac{1}{2}\sqrt[3]{\frac{6}{\pi}}\left[\sqrt[3]{v(x)} - \sqrt[3]{v(x) - l_\mathrm{e}(x)}\right]\tag{20}$$

Given this criterion, the full coagulation kernel K_{coag} ,which features the PBE (Equation (3)), can be formulated as

$$K_{\mathrm{coag}}(z, x_i, x_j) = K_{\mathrm{col}}(z, x_i, x_j)\mathbb{1}_{\{x_i, x_j | \mathrm{St_v}(x_i, x_j) \leq \mathrm{St_v^*}(x_i, x_j)\}}(x_i, x_j).\tag{21}$$

Following the approach of Goodson et al. [42], if a coagulation event is successful then a fraction of the external liquid l_e from the particles involved in the collision becomes internal liquid l_i in the newly formed particle. The pore volume of the newly formed particle is further modified for successful collisions. In this way, the coagulation transform is characterised, as in [24, 23], by the

13

following:

$$s_{\text{o}}(T_{\text{coag}}(x_i, x_j)) = s_{\text{o}}(x_i) + s_{\text{o}}(x_j) \tag{22}$$

$$l_{\text{e}}(T_{\text{coag}}(x_i, x_j)) = l_{\text{e}}(x_i) + l_{\text{e}}(x_j) - l_{\text{e}\to\text{i}}(x_i, x_j) \tag{23}$$

$$l_{\text{i}}(T_{\text{coag}}(x_i, x_j)) = l_{\text{i}}(x_i) + l_{\text{i}}(x_j) + l_{\text{e}\to\text{i}}(x_i, x_j) \tag{24}$$

$$p(T_{\text{coag}}(x_i, x_j)) = \frac{a_{\text{surf}}^+(x_i, x_j)^{\frac{3}{2}}}{6\pi^{1/2}} \tag{25}$$

$$- \left[s_{\text{o}}(x_i) + s_{\text{o}}(x_j) - l_{\text{e}}(x_i) - l_{\text{e}}(x_j) + l_{\text{e}\to\text{i}}(x_i, x_j) \right]$$

Here, $l_{\text{e}\to\text{i}}(x_i, x_j)$ represents the amount of surface liquid that is internalised due to the contact area between the colliding particle pair and $a_{\text{surf}}^+(x_i, x_j)$ is the surface area of the newly formed aggregate. Both of these terms are described in detail in [23].

Compaction

Several experimental studies [10, 18, 13, 43, 9] have concluded that internal liquid is squeezed to the surface of nuclei/nuclei fragments in areas of high compaction such as kneading blocks. This newly surfaced liquid then permits the layering of dry primary material onto the surface of the compacted particles. To described the movement of liquid during this squeezing process, some of the internal liquid is moved to external liquid. The amount of liquid transferred $l_{i\to e}$ is hypothesised to be proportional to the relative change in pore volume as described by the following relation:

$$l_{i\to e} = \Delta p_{\text{comp}} \left(\frac{l_{i,o}}{p_o} \right), \tag{26}$$

where $l_{i,o}$ and p_o are the internal liquid and pore volumes, respectively, prior to compaction and Δp_{comp} is the change in pore volume associated with a compaction event. Consistency between (1), (2) and (26) requires:

$$\Delta p_{\text{comp}} = p_o - \frac{\varepsilon_1 (s_{\text{o}} + l_{e,o} + l_{i,o})}{1 - \varepsilon_1 \left(1 - \frac{l_{i,o}}{p_o} \right)}. \tag{27}$$

Here, $l_{e,o}$ is the external liquid volume prior to compaction and ε_1 is the post compaction porosity. These relationships define the compaction transform T_{comp}.

14

Breakage

As in Braumann et al. [23], particles may undergo binary breakage and the daughter distribution is described by a beta distribution. The breakage transform is:

$$T_{\text{break}}(x_i) \rightarrow (x_j), (x_i - x_j), \tag{28}$$

where T_{break} is the breakage operator.

This rate of this process is controlled by fragmentation kernel F of Equation (3), which is formulated as [44]

$$F(z, x, \mathrm{d}y) = \mathbb{1}_{\{x,y|m(y)<m(x)\}}(x,y)g_{\text{break}}(z,x)B(x,y)\mathrm{d}y, \tag{29}$$

where $g_{\text{break}}(z,x)$ is the breakage frequency function and $B(x,y)$ is the probability measure on the space of fragments y for each parent particle x. In this way, $B(x,y)\mathrm{d}y$ is the probability that a fragmentation product from parent particle x exists within the space $[y, y + \mathrm{d}y]$.

The choice of breakage frequency function varies significantly across the literature, reflecting the relatively poor understanding of this particle process. Breakage kernels generally take the form of a power law, applied to the particle volume, which may have a fitted [30] or predefined exponent [28] and may also be partially dependent on the particle pore volume [23]. In preliminary model development, various power law kernels were tested and assessed through the PSD evolution of particles along the network. A volume-based kernel with direct proportionality was settled upon, due to its simplicity and the fact that it resulted in sensible PSD evolutions along the network. In the future, more complex breakage kernels could be investigated, with dependencies on particle properties such as the degree of compaction, internal liquid etc. and on screw geometry. Primary particles and particles with volume less than $v_{\text{parent}}^{\min}$ are considered to be unbreakable. The breakage frequency function for particle x

15

is:

$$g_{\text{break}}(z, x) = \begin{cases} k_{\text{att}}(z) n_{\text{screw}}^2(z) v(x), & \text{if } v(x) \geq v_{\text{parent}}^{\min} \text{ and } l_{\text{e}}(x) + l_{\text{i}}(x) + p(x) \neq 0, \\ 0 & \text{otherwise,} \end{cases}$$

(30)

where k_{att} is the attrition rate constant.

As in Braumann et al. [23], the product particles of a breakage event are assumed to have the same composition are the parent particle x. The volume of the fragment particle y is defined using the random variable [23]

$$v_y(z, x, \chi_{\text{frag}}) = v_{\text{frag}}^{\min} + \chi_{\text{frag}} \left[\nu_{\max} v(x) - v_{\text{frag}}^{\min} \right],$$

(31)

where $v_{\text{frag}}^{\min}$ is the minimum fragment volume that can be produced and $\nu_{\max}$ defines the maximum fraction of the parent particle which can break off. χ_{frag} is a random measure on the interval $[0, 1]$ with beta distribution [24]

$$f(\chi_{\text{frag}}) = \frac{1}{\Omega(\alpha_{\text{daughter}}, \beta_{\text{daughter}})} \chi_{\text{frag}}^{\alpha_{\text{daughter}} - 1} (1 - \chi_{\text{frag}})^{\beta_{\text{daughter}} - 1},$$

(32)

where

$$\Omega(\alpha_{\text{daughter}}, \beta_{\text{daughter}}) = \int_0^1 \chi_{\text{frag}}^{\alpha_{\text{daughter}} - 1} (1 - \chi_{\text{frag}})^{\beta_{\text{daughter}} - 1} d\chi_{\text{frag}}.$$

(33)

This characterises $B(x, y)$.

The total breakage rate R_{break} in compartment z is given by:

$$R_{\text{break}}(z, t) = \sum_{i=1}^{N(z,t)} g_{\text{break}}(z, x_i),$$

(34)

where $N(z, t)$ is the number of particles in compartment z at time t.

Penetration

As previously mentioned, binder penetration is modelled as a continuous processes within the model. The penetration process is intended to capture the flow of binder from the particle surface to the interior of the particle, driven by capillary forces. As in Braumann et al. [20] this involves the transformation of l_{e} to l_{i} at rate r_{pen}, controlled by the rate constant k_{pen} as:

$$r_{\text{pen}}(z, x) = k_{\text{pen}}(z) \mu_{\text{binder}}^{-1/2} l_{\text{e}}(x)(p(x) - l_{\text{i}}(x)),$$

(35)

16

where μ_{binder} is the viscosity of the binder.

Each particle in the ensemble is modified between stochastic jump events according to the following set of ordinary differential equations:

$$\frac{\mathrm{d}s_{\text{o}}}{\mathrm{d}t} = 0, \quad \frac{\mathrm{d}l_{\text{e}}}{\mathrm{d}t} = -r_{\text{pen}}, \quad \frac{\mathrm{d}l_{\text{i}}}{\mathrm{d}t} = r_{\text{pen}}, \quad \frac{\mathrm{d}p}{\mathrm{d}t} = -r_{\text{pen}}.$$

2.3. Compartmentalisation of the twin-screw
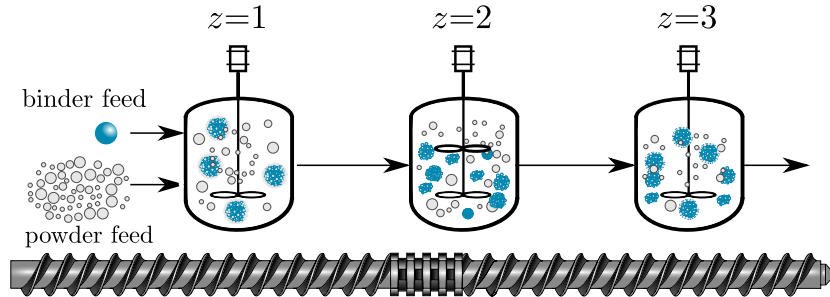
Figure 4: Compartmental representation of the twin-screw.

The experimental studies by Hagrasy et al. [16] were used to test the model. This study employed a screw configuration consisting of a conveying section followed by a section of conveying/kneading elements and then an additional conveying section. This is modelled as a series of three well-mixed compartments as illustrated in Figure 4. Compartments $z = 1$ and $z = 3$ are assumed to represent pure conveying sections, which are assumed to share the same set of rate constants. Droplet inception/nucleation is only permitted in the first compartment. The central conveying/kneading compartment ($z = 2$) is permitted to have different collision, breakage and compaction rates, relative to the pure conveying zones. The penetration rate is assumed to be a material constant and thus is the same in each compartment.

It is assumed that transformation of the feed material is limited prior to the point of liquid injection of the twin-screw system. For this reason the twin-screw system in modelled from the liquid injection point onwards.

17

In this study, each compartment is assumed to be of equal volume and thus, $V_{\text{real}}(z) = V_{\text{real,T}}/k_{\text{reac}}$ where k_{reac} is the number of compartments in the network and $V_{\text{real,T}}$ is the total volume of the TSG system.

Particle transport

The total rate of particle outflow from compartment $z \in \{1, 2, 3\}$ is given by:

$$R_{\text{outflow}}(z) = \frac{N(z, t)}{\tau(z)}, \tag{36}$$

where $\tau(z)$ is the characteristic residence time of compartment z. The rate of inflow into compartment $z + 1$ from compartment z is then given by:

$$R_{\text{inflow}}(z + 1, t) = \frac{V_{\text{samp}}(z + 1, t)}{V_{\text{samp}}(z, t)} R_{\text{outflow}}(z, t). \tag{37}$$

As in the work of Barrasso et al. [30] (which used the same experimental test case as that used in this study) the residence times are assumed to be equal in all compartments with $\tau = 2.67$s. In future work this assumption could be relaxed by incorporating information from experimental twin-screw residence time studies [31, 45] and PEPT investigations [36].

Particle Inception/Initialisation

Similar to liquid inception, the rate of inception of primary particles with form:

$$x_{\text{incept}}(d) = \left(\frac{\pi d^3}{6}, 0, 0, 0 \right) \tag{38}$$

into each compartment is given by:

$$I_{\text{solid}}(z, t, \mathrm{d}x) = \frac{\dot{M}_{\text{feed}} \mathbb{1}_{\{1\}}(z)}{V_{\text{real}}(z) \bar{m}_{\text{feed}}} q_{0, \mathbb{X}_{\text{incept}}}(x) \mathrm{d}x, \tag{39}$$

where and $\bar{m}_{\text{feed}}$ is the average arithmetic mass of the feed particles and $q_{0, \mathbb{X}_{\text{incept}}}$ is the distribution of incepted particles on the space $\mathbb{X}_{\text{incept}}$. The primary particle distribution for inception is derived from the volume fraction distribution $q_3(d)$ presented in [16] for the <u>Lactose Impalpable</u> excipient grade. Here, $q_3(d)\mathrm{d}d$ is fraction of the total particle volume contained within the size range d to $d + \mathrm{d}d$. This is converted into a number distribution $q_0(d)$ for use in the model using the relation [46]:

$$q_0(d) = \frac{q_3(d)d^{-3}}{\int_0^\infty q_3(d)d^{-3}\mathrm{d}d}. \tag{40}$$

18

$q_0(d)$ and $q_{0,\mathbb{X}_{\mathrm{incept}}}(x)$ are related as

$$q_{0,\mathbb{X}_{\mathrm{incept}}}(x_{\mathrm{incept}}(d)) = \frac{x_{\mathrm{incept}}(d)q_0(d)}{\int_{d_{\mathrm{min}}}^{d_{\mathrm{max}}} x_{\mathrm{incept}}(d)q_0(d)\mathrm{d}d}, \tag{41}$$

where d_{max} and d_{min} are the maximum and minimum particle diameters of the inception distribution, respectively.

Each compartment is assumed to be filled with primary particles at $t = 0$. The total rate of particle inception events is

$$R_{\mathrm{incept}}(z) = \begin{cases} \dot{M}_{\mathrm{feed}}/\bar{m}_{\mathrm{feed}}, & \text{if } z = 1, \\ 0, & \text{otherwise.} \end{cases} \tag{42}$$

3. Parameter estimation

The unknown rate constants (seven in total) are estimated using experimental PSDs from Hagrasy et al. [16] at LSR values of 0.15, 0.25 and 0.35 using the simulation parameters given in Table 1. The quality of the model fit against the experimental data is quantitatively measured using a weighted sum-of-squares objective function OF over all N_{exp} experimental conditions and N_{response} model/experimental responses as:

$$OF = \sum_{i=1}^{N_{\mathrm{exp}}} \sum_{j=1}^{N_{\mathrm{response}}} \left(\frac{y_{j,i}^{\mathrm{model}} - y_{j,i}^{\mathrm{exp}}}{\sigma_j} \right)^2. \tag{43}$$

Here, $y_{i,j}^{\mathrm{model}}$ is the jth model response for the ith LSR value used and $y_{j,i}^{\mathrm{exp}}$ is the associated experimental response. Mass based percentiles diameters d25, d50, d75 and d95 of the granular product are used as the model/experimental responses. These are weighted, respectively, using weighting factors σ of $25\mu\mathrm{m}$, $50\mu\mathrm{m}$, $75\mu\mathrm{m}$ and $95\mu\mathrm{m}$.

The geometry of the objective function is highly complex, containing multiple ridges and local minima. For this reason, we perform a quasi-random search over the parameter space, followed by a (more local) Hooke-Jeeves optimisation [50]. The initial search is carried out by generating a quasi-random sequence of rate constant vectors known as Sobol sequences [51]. Sobol sequences

19

Table 1: Summary of simulation parameters.

Parameter	Type	Value	Unit
d_{nozzle}	Operating parameter [16]	2×10^{-3}	m
$\dot{M}_{\mathrm{feed}}$	Operating parameter [16]	4.0	kg hr^{-1}
n_{screw}	Operating parameter [16]	6.67	rev s^{-1}
$V_{\mathrm{real,T}}$	Equipment geometry [47]	4.05×10^{-5}	m^3
e_{coag}	Material property (estimated)	0.2	-
ρ_{l}	Material property [48]	998	kg m^{-3}
ρ_{s}	Material property [49]	1545	kg m^{-3}
μ_{binder}	Material property [48]	10^{-3}	Pa s
d_{max}	Model parameter [16]	3.31×10^{-6}	m
d_{min}	Model parameter [16]	8.26×10^{-4}	m
h_{a}	Model parameter (estimated)	5×10^{-6}	m
k_{reac}	Model parameter (estimated)	3	-
s^*	Model parameter (estimated)	0.5	-
U_{col}	Model parameter (estimated)	0.3	m s^{-1}
$v_{\mathrm{frag}}^{\mathrm{min}}$	Model parameter (estimated)	8.18×10^{-12}	m^3
$v_{\mathrm{parent}}^{\mathrm{min}}$	Model parameter (estimated)	1.80×10^{-11}	m^3
$v_{\mathrm{nuc}}^{\mathrm{max}}$	Model parameter (estimated)	v_{drop}	m^3
$\alpha_{\mathrm{daughter}}$	Model parameter (estimated)	5.0	-
$\beta_{\mathrm{daughter}}$	Model parameter (estimated)	2.0	-
$\varepsilon_{\mathrm{bed}}$	Model parameter (estimated)	0.32	-
$\varepsilon_{\mathrm{min}}$	Model parameter (estimated)	0.5	-
ν_{max}	Model parameter (estimated)	0.5	-
τ	Model parameter [30]	2.76	s

are used in order to spread the model evaluation points more evenly across the parameter space. The Hooke-Jeeves algorithm is selected for the local optimisation since it is a 'derivative-free' optimisation technique. This characteristic is highly desirable in the context of this paper, since derivative approximation by finite differences is problematic with models whose response is subject to stochastic noise. Five Hooke-Jeeves optimisations are carried out, starting from each of the five best Sobol points (i.e. those with the lowest OF value).

Preliminary parameter estimation showed that very similar product PSDs could be obtained for very different sets of rates constants. For example, using the same wide search space for the breakage rate constant k_{att} in both the pure conveying and partial kneading section may result in a situation in which most of the breakage occurred in the conveying sections and very little in the partial kneading section and vice-versa, both giving relatively similar product PSDs. Since only the final PSD is used in the fitting process (mid-barrel experimental PSD data was not available), unphysical PSD evolutions along the network are not penalised by the objective function. Hence, such PSD evolutions must be eliminated through careful selection of the search space for each rate constant, reflecting what is know from experimental investigation. As previously discussed, the body of experimental TSG literature would suggest that the breakage and compaction rates in the kneading element and significantly higher than those present in pure conveying sections (though conveying section are known to break large agglomerates using a cutting action [8]). Thus, the parameter limits for k_{comp} and k_{att} in the central, partial kneading compartment ($z = 2$) are chosen such that they are higher than those of the pure conveying compartments ($z = 1, 3$). To assess the predictive power of the model, the optimised rate constants are then used to model two additional experimental cases with intermediate LSR values of 0.2 and 0.3 and the model parameters in Table 1.

The parameter estimation steps are carried out using the Model Development Suite (MoDS) [52]. MoDS is an advanced software package capable of analysing 'black-box' models.

21

Table 2: Rate constant bounds used in the parameter estimation process.

Compartment index z	1,3			2			1-3
Parameter	k_{col}	k_{att}	k_{comp}	k_{col}	k_{att}	k_{comp}	k_{pen}
Unit	m^3	m^{-3}s	-	m^3	m^{-3}s	-	$\text{kg}^{\frac{1}{2}}\text{m}^{-\frac{7}{2}}\text{s}^{-\frac{3}{2}}$
Lower bound	10^{-12}	1.68×10^4	0.01	10^{-12}	1.68×10^6	0.6	10
Upper bound	10^{-9}	1.68×10^7	0.6	10^{-9}	1.68×10^{10}	1.0	10^6
Scaling	Log	Log	Linear	Log	Log	Linear	Log

4. Results and discussion

In this section we present the simulation results using the optimised rate constants derived from parameter estimation. In Section 4.1 we analyse the model results in the context of the experimental data at LSR values used in the fitting and at a number of intermediate LSR values. This is followed by an analysis of the model PSD evolution along the length of the screw barrel in Section 4.2.

The product ensembles are sieved using a sieve set starting from 32μm to 8064μm using a $\sqrt{2}$ geometric progression. Sieve mass fractions are plotted against the mid-point of the corresponding sieve intervals. Statistical errors estimations for these parameters are reported as 90% confidence intervals.

4.1. The effect of liquid flowrate on particle size distribution

A comparison between the model and experimental product PSD is presented in Figure 5. There is an obvious trend in the results where by the intensity of the primary particle mode is reduced with increasing LSR, leading to a reduction in the fines and a larger mean granule size, as observed in TSG experiments [53, 35, 18]. The main disparities occur at higher LSR values where the largest particles size classes produced in the experiment are not captured by the model. The model PSD is bimodal in all cases, consisting of a primary

particle mode and an additional mode composed of nuclei fragments which have gone through breakage, coagulation and compaction processes. Such bimodality is generally a feature of TSG product PSD. Hagrasy et al. [16] hypothesised that the inherently bimodal nature of the twin-screw device was a result of the liquid addition method, resulting in a non-uniform liquid distribution, in agreement with the results of [17]. In contrast, Vercruysse et al. [9] concluded that the biomodality was not primarily induced by insufficient mixing of the powder and liquid phases, and was instead a result of the granulation mechanism inherent to TSG. This was supported by the experiments carried out by Fonteyne et al. [54] and Vercruysse et al. [55]. El Hagrasy and Litster [10] also observed that the liquid distribution becomes more uniform with the addition of more kneading blocks. The experimental PSD for low to moderate LSR in Figure 5 may well be evolved from a more pronounced bimodal distribution, with a degree of overlap between the modes. Such a distribution would be subjected to reduction in intensity along the barrel length. The current model appears to fail in capturing some of the more subtle processes that lead to the mitigation of this bimodality, even in the presence of relative few kneading elements.

There is a clear over-prediction of fines by the model at high LSR values (Figure 5(c) and 5(e)). This may indicate the need for a layering mechanism in the model. This would allow primary particles to become attached to the surface of larger, surface wet agglomerates as a rapid continuous process or additional particle jump process. This would ultimately lead to the separate treatment of the rates/particle transforms associated with agglomerate-primary and agglomerate-agglomerate collisions. Such layering mechanisms have been implemented in the context of a sectional TSG model by Barrasso and Ramachandran [39] and a stochastic model for a high-shear batch mixer by Oullion et al. [56]. The failure to produce the pronounced peak at 4000μm in the case where LSR=0.3 may also indicate that a less aggressive/more versatile breakage kernel (possibly with a variable volume exponent) may be required in the future. This peak may also correspond to particles which have become strengthened through compaction in the kneading elements. Again, such struc-

23

tural changes may need to introduced into the breakage functional to capture the resistance of such particles to further breakage.

Moving to the lower LSR operating range, the disparity between model and experiment in the lowest sieve classes (Figures 5(a) and 5(d)) indicates that, in the real system, large primary particles and/or agglomerates may undergo attrition along the barrel length, therefore acting as a source of 'fines'. Another possible explanation for this discrepancy is that preferential incorporation of larger primary particles in the nucleation mechanism of the model in more pronounced that it is in the real system. Dhenge et al. [13] showed that the material in the barrel became less cohesive with decreasing LSR, resulting in a material that was less resistant to flow and subject to shorter residence times (though this was only tested to LSR values as low as 0.25). This reduction in residence time indicates a lower degree of barrel filling at lower LSR values and may, as suggested by Thompson and Sun [57], result in the material not being protected from the high shear zone at the barrel wall, causing subsequent attrition of largest primary particles in the low LSR regime. Since the breakage of dry primary particles is distinct from the breakage of wet agglomerates, (which may be able to deform and elongate) it is likely that distinct breakage models are required to accurately capture the breakage process for each phase.

Across the complete LSR operating range, the discrepancies between the model and experimental PSD in Figure 5 may have been affected, to some degree, by the varying aspect ratio of particles produced experimentally. It is known that the aspect ratio of particles generally decreases with increasing LSR producing more rounded particles [53, 13, 58], however, as demonstrated by Hagrasy et al. [16], this breaks down at very high LSR. At this high LSR operating range, long extrudate like particle are produced as the mixture becomes more of a paste, making the geometrical variations particularly hard to capture from a modelling perspective. Ultimately, the presence of particles with high aspect ratios may skew the sieve analysis, depending on the particle orientation. It will also affect the nature of subsequent particle breakage and growth. In the current model, particles are considered to be spherical. More complex particle

24

descriptions with element-specific shape transformations may need to be taken into account in future modelling works. Due to the highly extensible nature of stochastic models, it is possible to track such additional features without significantly affecting the computational cost of the solution process. Nevertheless, work would be required to elucidate the effects of each type of element and how these effects depend on the properties of the particles involved.

Another potential source of error in the model is the assumption of equal residence times across all compartments. As TSG Positron Emission Particle Tracking (PEPT) studies have shown [59, 36], the material fill ratio before/in the kneading block is generally greater than that in the final conveying zone. This would extend the residence time of the kneading block and thereby reduce the time spent by particles in conveying sections. The fill level is known to play an important role in determining the shape and size of the particles since this determines the degree of compaction [58] and, again, may also protect particles from contacting the high shear boundary between the wall and the screw, thereby mitigating breakage [57]. This variation in mass distribution could be incorporated into the model by way of a flow model (such as that done for hot melt extrusion by Eitzlmayr et al. [60]) or, alternatively, by coupling the population balance to simulations using the Discrete Element Method (DEM), though such DEM couplings come at a high computational cost.

4.2. Evolution of the particle size distribution along the barrel

In this section the evolution of the model PSD is assessed along the length of the network (or equivalently, the length of the barrel) for an operating LSR of 0.25. Figure 6 shows the PSD in each compartment along the network and Table 3 details the optimised rate constants for each compartment.

We see that the dominant mechanism in the first compartment ($z = 1$) is nucleation, which causes a pronounced peak in the PSD around 2500μm. As a result of the bounds used for parameter estimation, in Table 3 we see that conveying-only compartments ($z = 1, 3$) are subject to a lower degree of breakage (k_{att}) relative to the compartment containing the kneading elements

25

$(z = 2)$. The reduced breakage rate allowed the oversized nucleates to co-exist with the remaining primary powder in a highly bimodal distribution, alluding to the inherent bimodality-by-liquid-inception suggested by Hagrasy et al. [16] and observed by [17]. The position of the nuclei peak relative to the droplet size of 2000μm indicates that nuclei have been subjected to a moderate degree of compaction in the first compartment following their formation.

Moving from $z = 1$ to $z = 2$ in Figure 6, we see that a high degree of compaction and breakage has broken down the large nuclei into smaller, more dense fractions, consistent with the findings of Djuric and Kleinebudde [61]. We also note that the penetration rate constant has reached it's lower bound and this [process has effectively turned of. This is likely a reflection of the competition between the compaction and penetration processes in. These processes compete to move liquid to and from the surface of the particles, respectively. Thus the amount of surface liquid available during coagulation events is not sensitive to the absolute the value of k_{comp} and k_{pen} but rather their relative magnitudes. This coupling is undesired and is areas in which the model could be improved upon in the future. The squeezing effects of the compaction processes are further evident from the average particle composition statistics (Figure 7), in which a slight reduction in internal liquid (and resulting increase in external liquid) is evident in the transition between $z = 1$ and $z = 2$. This replicates the squeezing process within kneading blocks observed in numerous experimental studies [10, 18, 13, 43, 9].

It is also noted that breakage is the dominant process in the second compartment (kneading zone) and that the coagulation rate constant has reached it's lower bound, indicating very limited coagulation within this compartment. It is likely that similar ratios of k_{att} to k_{col} could feasibly generate similar size distributions within $z = 2$ due to the competing nature of the coagulation and breakage processes.

As the particles transition from the kneading zone to the final conveying zone, we observe a degree of coalescence between primary particles and compacted/surface wet agglomerates. At this stage the combination of moderate

26

breakage and low compaction rate allows particles to grow whilst increasing in porosity (the reader is reminded that successful coalescence events result in an increase in particle pore volume in the model). This is in line with the production of large <u>friable</u> agglomerates from conveying only section observed in TSG and twin-screw extrusion systems [61].

Table 3: Optimised rate constants.

Compartment index z	1,3			2			1-3
Parameter	k_{col}	k_{att}	k_{comp}	k_{col}	k_{att}	k_{comp}	k_{pen}
Unit	m^3	m^{-3}s	-	m^3	m^{-3}s	-	kg$^{\frac{1}{2}}$m$^{-\frac{7}{2}}$s$^{-\frac{3}{2}}$
Value	1.21×10^{-10}	9.42×10^{6}	0.395	9.99×10^{-13}	1.09×10^{9}	0.954	10.0

4.3. Model sensitivity

In this section the sensitivity of the resulting model to two main input parameters, namely the droplet diameter d_{drop} and the collision rate constant k_{col} are investigated.

4.3.1. Droplet diameter

From the results in Section 4.1, Figure 5, it is noted that the agglomerate mode of the simulated PSD response did not, as in the case of the experiments, shift to right with increasing LSR. The shift in the experimental response could be indicative of the the re-wetting of agglomerates in the liquid zone when the liquid flowrate is significantly high. To attempt to capture this feature within the model, an effective droplet size is determined from each experimental response (for each LSR). The effective droplet size is indirectly estimated from the approximated centre of the agglomerate mode in each experimental response. Let x_{agg} be an estimate of the representative particle that takes position at the centre of the agglomerate mode in experimental PSD response. Let the

27

diameter of this particle be denoted d_{agg}. Suppose that x_{agg} approximately the same composition as a nuclei particle, such that

$$x_{\mathrm{agg}} = \left(\frac{\pi d_{\mathrm{drop}}}{6\phi_{\mathrm{max}}}, 0, \frac{\pi d_{\mathrm{drop}}}{6}, \frac{\pi d_{\mathrm{drop}}}{6s^*} \right),\tag{44}$$

then, by way of the volume definition 1, an effective droplet size d_{drop} can be expressed as

$$d_{\mathrm{drop}} = d_{\mathrm{agg}} \left(\phi_{\mathrm{max}}^{-1} + s^{*-1} \right)^{-\frac{1}{3}} \approx 0.699 d_{\mathrm{agg}}.\tag{45}$$

Of course the above treatment neglects the effects of compaction and breakage on this mode along the barrel length, nevertheless, it will suffice to generate sensible droplet diameters with which to test the sensitivity of the model response. Using (45) to generate effective droplet diameters, simulations were carried out for LSR values 0.15, 0.2, 0.25, 0.3 and 0.35. All simulations were carried out using the optimised rate constants presented in Table 3. The resulting simulation responses are presented in Figure 8 in conjunction with the simulation responses for the default droplet diameter of 2mm (used in the fitting procedure). From the results, it is observed that the change in droplet diameter has caused moderate changes to the shape of the primary particle mode, though these changes are generally within the confidence bands of the respective responses. In terms of the agglomerate mode, moderate changes intensity of the peak are observed for very low and very high LSR values, however, the position of this mode has not significantly shifted. Only a minor shift is noted in the agglomerate mode for high LSR and where the effective droplet size was increased by 0.8mm. The insensitivity of the model to the droplet diameters is mostly likely explained by a combination of the breakage and compaction dynamics. It was previously observed from the PSD evolution in Figure 6 that there is a significant shift in the agglomerate mode along the compartmental network of the simulation. The final position of the agglomerate mode is therefore a balance between the compaction, breakage and coagulation processes. Since the rate constants associated with these process do not differ between the new simulations and the reference simulation presented in Figure 8, the effect of altering the droplet size

28

on resulting PSD is minimal.

4.3.2. Collision rate

In light of the under-prediction of fines consumption in the fitted experimental responses of Figure 5, particularly at high LSR, it is worth exploring the effect of increasing the collision rate constants k_{col} on the simulation response. It is expected that increased collision rates should promote increase the coagulation rate between the agglomerate and fines modes, provided there is sufficient surface liquid available to facilitate the formation of liquid bridges between the colliding species. A number of simulations were carried out in which the set of fitted collision rate constants (see Table 3) was increased (scaled by the same factor in each compartment). The maximum collision rate tested for $z = 1, 3$ was $1.21 \times 10^{-8} \mathrm{m}^3$, which greatly exceeds the upper bound used in the parameter optimisation procedure. For all other rate parameters, the values in Table 3 were employed in conjunction with the LSR-dependent effective droplet sizes given in Figure 8. The resulting simulation responses are compared in Figure 9. As expected, in all cases, increasing in the collision rate constants has promoted the consumption of fines and increased the intensity of the agglomerate mode. Though the resulting model fits with the experimental data have significantly improved for high LSR values (0.3, 0.35), this has come at the expense of a reduced quality of fit at low LSRs. The level of fines consumption at LSRs in the range 0.15-0.25 is much greater than that observed experimentally. Though an overall poor fit quality is expected for the simulations with modified coagulation rates (since the other rate constants have not been re-estimated), the results nevertheless indicate that competition of processes that controls the level of surface liquid, namely compaction (currently driven by collision processes) and liquid penetration, may need to re-visited in future modelling efforts.

(a) LSR=0.15

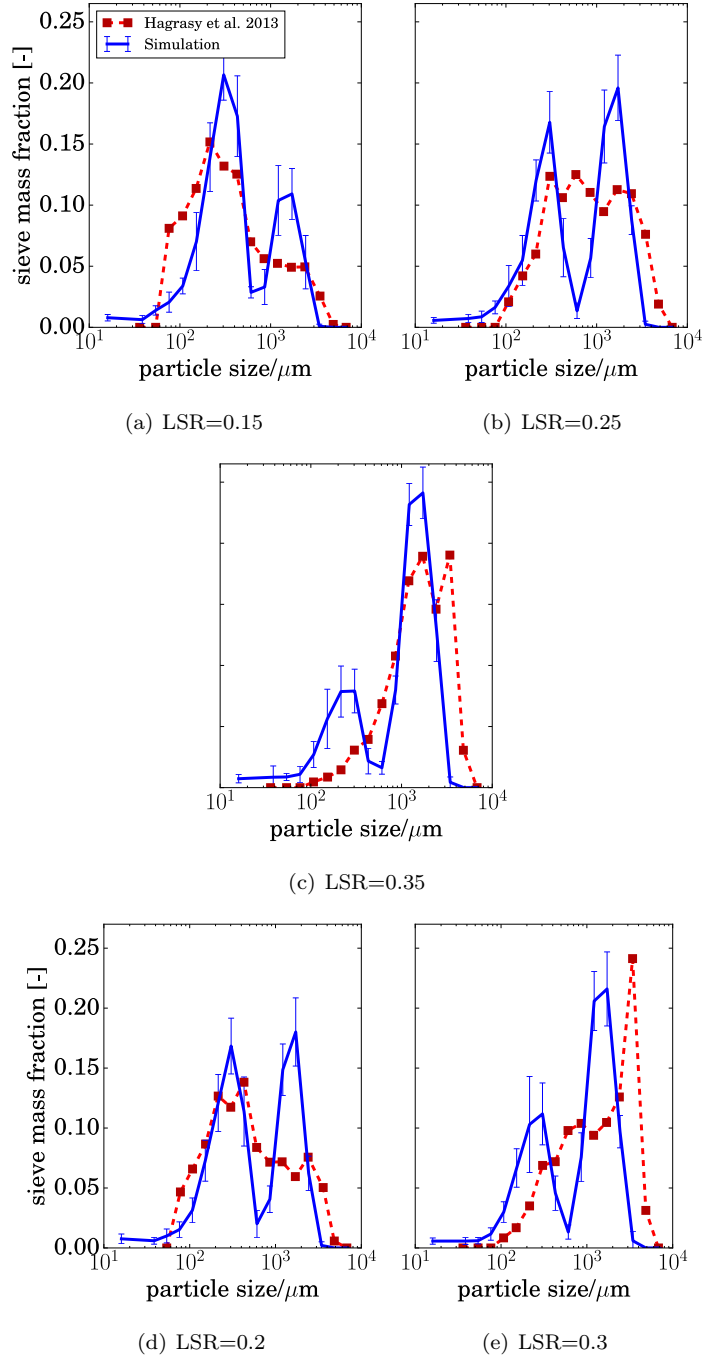(b) LSR=0.25

(c) LSR=0.35

(d) LSR=0.2

(e) LSR=0.3

Figure 5: Simulation PSDs compared with the experimental results of Hagrasy et al. [16]. LSR values which were used in the fitting of the rate constants are presented in (a)-(c) and 'blind tested' intermediate LSR values in (d) and (e).
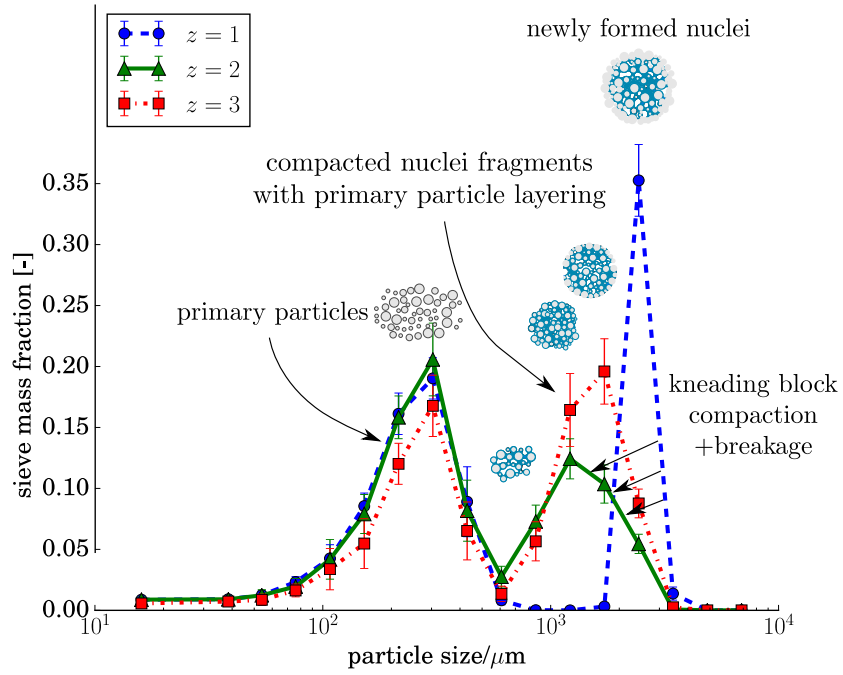
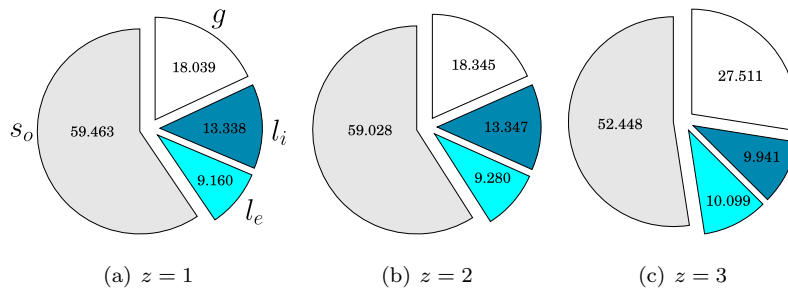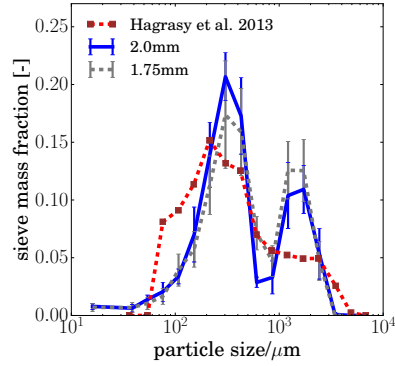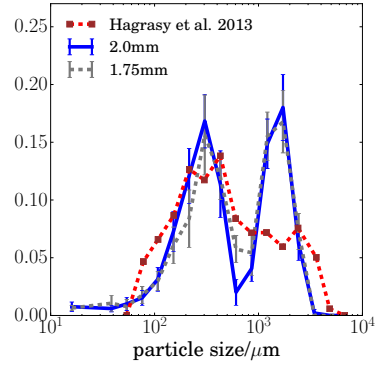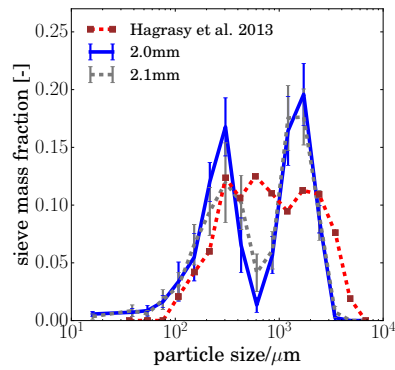Figure 6: Spatial PSD evolution for simulation with LSR=0.25.

(a) $z = 1$ (b) $z = 2$ (c) $z = 3$

Figure 7: Number averaged particle composition along the length of the compartment network with with an operating LSR=0.25.
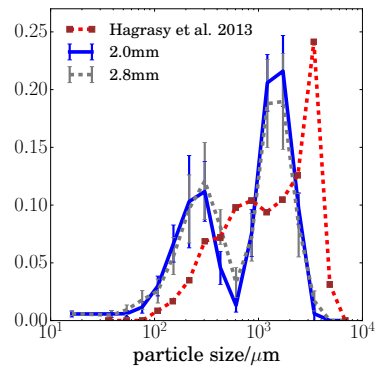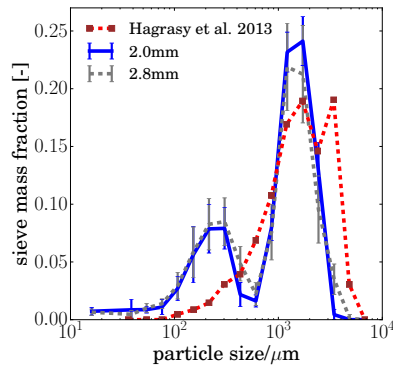
(a) LSR=0.15
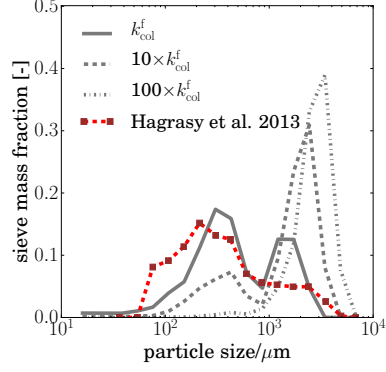
(b) LSR=0.2
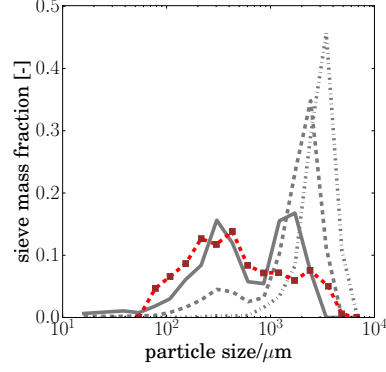
(c) LSR=0.25

(d) LSR=0.3

(e) LSR=0.35

Figure 8: Simulation PSDs compared with the experimental results of Hagrasy et al. [16] using the default droplet size of 2mm (blue trace) and hypothesised effective droplet size for each LSR (grey trace). All simulations were carried out with the calibrated rate constants in Table 3.
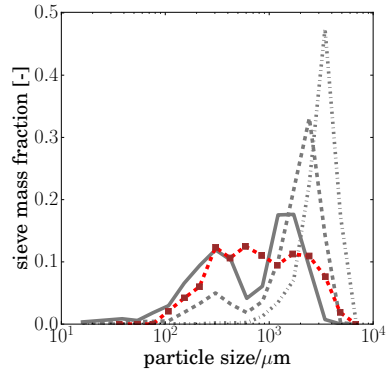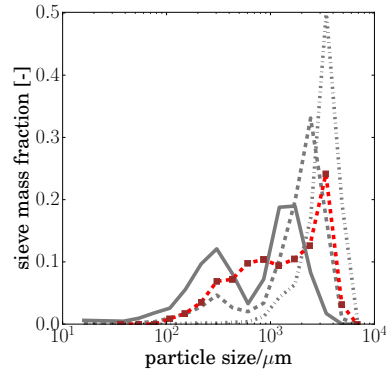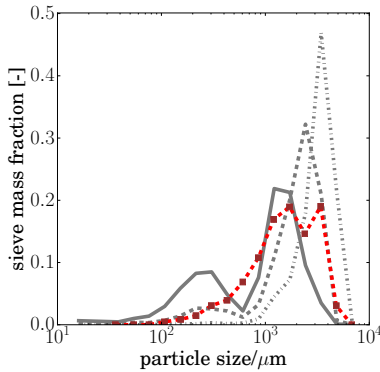
(a) LSR=0.15, d_{drop}=1.75mm

(b) LSR=0.2, d_{drop}=1.75mm

(c) LSR=0.25, d_{drop}=2.1mm

(d) LSR=0.3, d_{drop}=2.8mm

(e) LSR=0.35, d_{drop}=2.8mm

Figure 9: Simulation PSDs compared with the experimental results of Hagrasy et al. [16] for varying collision rate constants sets $[k_{\mathrm{col}}(1), k_{\mathrm{col}}(2), k_{\mathrm{col}}(3)]$. Each simulation uses the effective droplet sizes for each LSR, shown in the sub-captions. Here, $k_{\mathrm{col}}^{\mathrm{f}}$ represents the set of fitted collision rate constants presented in Table 3. Where collision rates have been scaled, the fitted value of k_{col} in Table 3 has been scaled by the same factor in all compartments.

5. Conclusions and future recommendations

In this paper we have presented a high dimensional model for TSG which includes particles coagulation, compaction, breakage, penetration and nucleation. The model performed reasonably well against experiment at low LSR values but showed an over-prediction of fines at higher LSR values, resulting in a consistently bimodal PSD. It was demonstrated that the model response had low sensitivity to the incepted droplet size and that the simulated product PSD was highly sensitive to value of the coagulation rate constant employed.

Based on the results of this study a number of recommendations for model improvements and future analysis can be made. Firstly, the introduction of a layering mechanism may mitigate the over-prediction of fines by the current model. This may also better reflect the difference between collision events involving a mixture of primary particles and agglomerates and those between agglomerates alone. Consideration of variable particle aspect ratios may be required to reflect the experimentally observed particle elongation. This is important both in the sieving process and in determining the likelihood of particle breakage/the resulting daughter distribution. It is also suggested that the population balance be coupled to a method for prediction of the mass distribution along the barrel from which compaction rates and residence times may be estimated. Finally, in order for optimised rates to be 're-used' across varying screw configurations the fitting methodology itself must be improved upon. In the future more advanced parameter optimisation could be carried out by fitting each compartmental PSD of the model against the experimental PSD at each associated barrel position, as carried out experimentally by Kumar et al. [58]. However, non-destructive extraction of a representative sample mid-barrel can be challenging. Alternatively, the model could be optimised against a large number of experiments with varying screw configuration (such as that carried out by Vercruysse et al. [9]), in order to isolate the individual contributions of each group of elements. Another option is to perform optimisation of element specific rate constants based on experimental studies such as that by Sayin et al.

[11]. Here the role of each element types is assessed by only supplying liquid at the very end of the barrel, such that only a short section of the twin-screw is active and the compounded effects of different elements in sequence are mitigated. However, it is likely that the role of specific screw elements is inherently coupled to the complete screw configuration and other processing conditions. It is more likely that a combination of these approaches will be required to build and refine future TSG models, gather element specific rate constants and move towards a truly modular TSG modelling framework.

Nevertheless, the stochastic method employed in the solution of this model, unlike traditional sectional methods, allows the dimensionality of the particle description to be readily extended to include many of the features that have been described above. These additional properties may then be incorporated into the particle transformations associated with TSG mechanisms. This makes this work an important step towards a quantitative prediction tool for formulation development with TSG systems.

In the second part of this study we present and analyse the properties of the numerical methodology employed to overcome the numerical challenges presented by twin-screw systems and solve the model presented in this paper.

Acknowledgements

Nomenclature

Roman symbols

B	breakage fragment distribution	-
d	particle diameter	m
d_{max}	maximum primary particle diameter	m
d_{min}	minimum primary particle diameter	m
F	breakage kernel	s^{-1}
g_{break}	breakage frequency	s^{-1}
h_{l}	thickness of external binder layer	m
I_{drop}	droplet inception rate	$\mathrm{s}^{-1}\mathrm{m}^{-3}$
I_{solid}	solid inception rate	$\mathrm{s}^{-1}\mathrm{m}^{-3}$
k_{att}	breakage rate constant	$\mathrm{s}\ \mathrm{m}^{-3}$
k_{col}	collision rate constant	m^3
k_{comp}	compaction rate constant	-
k_{nuc}	nucleation rate constant	s^{-1}
k_{pen}	penetration rate constant	$\mathrm{kg}^{1/2}\mathrm{m}^{-7/2}\mathrm{s}^{-3/2}$
k_{reac}	number of compartments	-
K_{coag}	coagulation kernel	$\mathrm{m}^3\mathrm{s}^{-1}$
K_{col}	size independent collision kernel	$\mathrm{m}^3\mathrm{s}^{-1}$
K_{nuc}	nucleation kernel	$\mathrm{m}^3\mathrm{s}^{-1}$
l_{e}	external liquid volume	m^3
l_{i}	internal liquid volume	m^3
$l_{\mathrm{i}\to\mathrm{e}}$	volume of liquid transferred to exterior during compaction	m^3
LSR	operating liquid solid mass flowrate ratio	-
$\tilde{m}$	harmonic mean particle mass	kg
$\bar{m}_{\mathrm{feed}}$	number average feed particle mass	kg
$\dot{M}_{\mathrm{feed}}$	solid mass flowrate	$\mathrm{kg}\ \mathrm{s}^{-1}$

n_{screw}	screw speed	rev s^{-1}
N	number of particles	-
N_{exp}	number of experimental conditions	-
N_{response}	number of simulation/experimental responses	-
OF	fitting objective function	-
p	pore volume	m^3
Δp_{comp}	compaction pore reduction	m^3
q_0	primary particle number distribution	m^{-1}
$q_{0,\mathbb{X}_{\text{incept}}}$	primary particle number distribution on $\mathbb{X}_{\text{incept}}$	-
q_3	primary particle volume distribution	m^{-1}
r_{pen}	particle penetration rate	m^{3}s^{-1}
$\tilde{R}$	harmonic mean particle radius	m
R_{incept}	primary particle inception rate	s^{-1}
$R_{,\text{droplet}}$	droplet inception rate	s^{-1}
R_{inflow}	particle inflow rate	s^{-1}
R_{nuc}	nucleation rate	s^{-1}
R_{outflow}	particle outflow rate	s^{-1}
s_{o}	original solid volume	m^3
s^*	pore saturation limit	-
t	time	s
T_{break}	breakage operator	-
T_{coag}	coagulation transform	-
T_{comp}	compaction transform	-
T_{nuc}	nucleation growth transform	-
U_{col}	particle collision velocity	m s^{-1}
v	particle volume	m^3
$v_{\text{nuc}}^{\text{max}}$	maximum particle volume permitted to join nucleus	m^3

$v_{\text{parent}}^{\min}$	minimum volume for breakage	m^3
v_{drop}	droplet volume	m^3
V_{real}	compartment volume	m^3
$V_{\text{real,T}}$	total volume of all compartments	m^3
V_{samp}	compartment sample volume	m^3
$\dot{V}_l$	binder flowrate	m^{3}s^{-1}
x	particle vector	m^3
x_{drop}	droplet particle vector	m^3
x_{nuc}	nuclei particle vector	m^3
y_{exp}	experimental fitting response	m
y_{sim}	simulation fitting response	m
z	compartment index	-

Greek symbols

α_{daughter}	breakage distribution parameter	-
β_{daughter}	breakage distribution parameter	-
ε	particle porosity	-
ε_{bed}	particle bed packing fraction	-
$\varepsilon_{\min}$	minimum particle porosity	-
μ_{binder}	binder viscosity	Pa s
λ	concentration measure	m^{-3}
ν	breakage product parameter	-
ρ_{l}	binder density	kg m^{-3}
ρ_{l}	solid density	kg m^{-3}
ϕ	liquid saturation	-
$\phi_{\max}$	maximum liquid saturation	-
σ	fitting response scaling factor	m
τ	compartment residence time	s

ϕ	test function	-
χ_{frag}	breakage parameter	-

References

1. Iveson SM, Litster JD, Hapgood K, Ennis BJ. Nucleation, growth and breakage phenomena in agitated wet granulation processes: a review. Powder Technology 2001;117(1-2):3 – 39. doi:`10.1016/S0032-5910(01)00313-8`.

2. Braumann A, Kraft M. Incorporating experimental uncertainties into multivariate granulation modelling. Chemical Engineering Science 2010;65(3):1088 –100. doi:`10.1016/j.ces.2009.09.063`.

3. Tu WD, Ingram A, Seville J. Regime map development for continuous twin screw granulation. Chemical Engineering Science 2013;87:315 –26. doi:`10.1016/j.ces.2012.08.015`.

4. Shah U. Use of a modified twin-screw extruder to develop a high-strength tablet dosage form. Pharmaceutical technology 2005;29(6):52–66.

5. Cartwright JJ, Robertson J, D'Haene D, Burke MD, Hennenkamp JR. Twin screw wet granulation: Loss in weight feeding of a poorly flowing active pharmaceutical ingredient. Powder Technology 2013;238:116 –21. doi:`10.1016/j.powtec.2012.04.034`.

6. Vercruysse J, Peeters E, Fonteyne M, Cappuyns P, Delaet U, Assche IV, Beer TD, Remon J, Vervaet C. Use of a continuous twin screw granulation and drying system during formulation development and process optimization. European Journal of Pharmaceutics and Biopharmaceutics 2015;89:239 –47. doi:`10.1016/j.ejpb.2014.12.017`.

7. Ge W, Han Y, Wang J, Wang L, Liu X, Zhou J, Li J, Freeman T, Birkmire A, Armstrong B. A QbD approach to continuous tablet manufacture.

39

Procedia Engineering 2015;102:443 –9. doi:10.1016/j.proeng.2015.01.185.

8. Lute SV, Dhenge RM, Hounslow MJ, Salman AD. Twin screw granulation: Understanding the mechanism of granule formation along the barrel length. Chemical Engineering Research and Design 2016;110:43 – 53. doi:10.1016/j.cherd.2016.03.008.

9. Vercruysse J, Burggraeve A, Fonteyne M, Cappuyns P, Delaet U, Assche IV, Beer TD, Remon J, Vervaet C. Impact of screw configuration on the particle size distribution of granules produced by twin screw granulation. International Journal of Pharmaceutics 2015;479(1):171 –80. doi:10.1016/j.ijpharm.2014.12.071.

10. El Hagrasy AS, Litster JD. Granulation rate processes in the kneading elements of a twin screw granulator. AIChE Journal 2013;59(11):4100–15. doi:10.1002/aic.14180.

11. Sayin R, Hagrasy AE, Litster J. Distributive mixing elements: Towards improved granule attributes from a twin screw granulation process. Chemical Engineering Science 2015;125:165 –75. doi:10.1016/j.ces.2014.06.040.

12. Dhenge RM, Cartwright JJ, Doughty DG, Hounslow MJ, Salman AD. Twin screw wet granulation: Effect of powder feed rate. Advanced Powder Technology 2011;22(2):162 –6. doi:10.1016/j.apt.2010.09.004.

13. Dhenge RM, Cartwright JJ, Hounslow MJ, Salman AD. Twin screw wet granulation: Effects of properties of granulation liquid. Powder Technology 2012;229:126 –36. doi:10.1016/j.powtec.2012.06.019.

14. Li H, Thompson M, O'Donnell K. Examining drug hydrophobicity in continuous wet granulation within a twin screw extruder.

International Journal of Pharmaceutics 2015;496(1):3 – 11. doi:`10.1016/`
`j.ijpharm.2015.07.070`.

15. Vanhoorne V, Bekaert B, Peeters E, Beer TD, Remon JP, Vervaet C. Improved tabletability after a polymorphic transition of delta-mannitol during twin screw granulation. International Journal of Pharmaceutics 2016;506(1-2):13 – 24. doi:`10.1016/j.ijpharm.2016.04.025`.

16. Hagrasy AE, Hennenkamp J, Burke M, Cartwright J, Litster J. Twin screw wet granulation: Influence of formulation parameters on granule properties and growth behavior. Powder Technology 2013;238:108 –15. doi:`10.1016/` `j.powtec.2012.04.035`.

17. Saleh MF, Dhenge RM, Cartwright JJ, Hounslow MJ, Salman AD. Twin screw wet granulation: Binder delivery. International Journal of Pharmaceutics 2015;487(1-2):124 –34. doi:`10.1016/j.ijpharm.2015.04.017`.

18. Seem TC, Rowson NA, Ingram A, Huang Z, Yu S, de Matas M, Gabbott I, Reynolds GK. Twin screw granulation - a literature review. Powder Technology 2015;276:89 – 102. doi:`10.1016/j.powtec.2015.01.` `075`.

19. Ramkrishna D. Population Balances: Theory and Applications to Particulate Systems in Engineering. Elsevier Science; 2000.

20. Braumann A, Man PLW, Kraft M. Statistical approximation of the inverse problem in multivariate population balance modeling. Journal of Industrial and Engineering Chemistry 2010;49(1):428–38. doi:`10.1021/ie901230u`.

21. Braumann A, Kraft M, Mort PR. Parameter estimation in a multidimensional granulation model. Powder Technology 2010;197(3):196 – 210. doi:`10.1016/j.powtec.2009.09.014`.

22. Braumann A, Man PLW, Kraft M. The inverse problem in granulation modeling-two different statistical approaches. AIChE Journal 2011;57(11):3105–21. doi:`10.1002/aic.12526`.

23. Braumann A, Kraft M, Wagner W. Numerical study of a stochastic particle algorithm solving a multidimensional population balance model for high shear granulation. Journal of Computational Physics 2010;229(20):7672 – 91. doi:`10.1016/j.jcp.2010.06.021`.

24. Braumann A, Goodson MJ, Kraft M, Mort PR. Modelling and validation of granulation with heterogeneous binder dispersion and chemical reaction. Chemical Engineering Science 2007;62(17):4717 –28. doi:`10.1016/j.ces.2007.05.028`.

25. Kastner CA, Brownbridge GP, Mosbach S, Kraft M. Impact of powder characteristics on a particle granulation model. Chemical Engineering Science 2013;97:282 –95. doi:`10.1016/j.ces.2013.04.032`.

26. Barrasso D, Tamrakar A, Ramachandran R. Model order reduction of a multi-scale PBM-DEM description of a wet granulation process via ANN. Procedia Engineering 2015;102(Supplement C):1295 –304. doi:`doi.org/10.1016/j.proeng.2015.01.260`.

27. Chaudhury A, Armenante ME, Ramachandran R. Compartment based population balance modeling of a high shear wet granulation process using data analytics. Chemical Engineering Research and Design 2015;95:211 – 28. doi:`10.1016/j.cherd.2014.10.024`.

28. Kumar A, Vercruysse J, Mortier ST, Vervaet C, Remon JP, Gernaey KV, Beer TD, Nopens I. Model-based analysis of a twin-screw wet granulation system for continuous solid dosage manufacturing. Computers & Chemical Engineering 2016;89:62 – 70. doi:`10.1016/j.compchemeng.2016.03.007`.

29. Barrasso D, Eppinger T, Pereira FE, Aglave R, Debus K, Bermingham SK, Ramachandran R. A multi-scale, mechanistic model of a wet granulation process using a novel bi-directional PBM-DEM coupling algorithm. Chemical Engineering Science 2015;123:500 –13. doi:`10.1016/j.ces.2014.11.011`.

30. Barrasso D, Hagrasy AE, Litster JD, Ramachandran R. Multi-dimensional population balance model development and validation for a twin screw granulation process. Powder Technology 2015;270, Part B:612 –21. doi:`10.1016/j.powtec.2014.06.035`.

31. Kumar A, Vercruysse J, Toiviainen M, Panouillot PE, Juuti M, Vanhoorne V, Vervaet C, Remon JP, Gernaey KV, Beer TD, Nopens I. Mixing and transport during pharmaceutical twin-screw wet granulation: Experimental analysis via chemical imaging. European Journal of Pharmaceutics and Biopharmaceutics 2014;87(2):279 –89. doi:`10.1016/j.ejpb.2014.04.004`.

32. Hounslow MJ, Ryall RL, Marshall VR. A discretized population balance for nucleation, growth, and aggregation. AIChE Journal 1988;34(11):1821–32. doi:`10.1002/aic.690341108`.

33. Lee KF, Mosbach S, Kraft M, Wagner W. A multi-compartment population balance model for high shear granulation. Computers & Chemical Engineering 2015;75:1 – 13. doi:`10.1016/j.compchemeng.2015.01.009`.

34. Patterson RIA, Singh J, Balthasar M, Kraft M, Norris J. The linear process deferment algorithm: A new technique for solving population balance equations. SIAM Journal on Scientific Computing 2006;28(1):303–20.

35. Dhenge RM, Cartwright JJ, Hounslow MJ, Salman AD. Twin screw granulation: Steps in granule growth. International Journal of Pharmaceutics 2012;438(1-2):20 – 32.

36. Seem TC, Rowson NA, Gabbott I, de Matas M, Reynolds GK, Ingram A. Asymmetric distribution in twin screw granulation. European Journal of Pharmaceutics and Biopharmaceutics 2016;106:50 – 8. doi:10.1016/j.ejpb.2016.01.013.

37. Meggle excipients and technology. https://www.meggle-pharma.com/en/productConfigurator.html; 2018. Accessed: 2018-01-30.

38. Vonk P, Guillaume C, Ramaker J, Vromans H, Kossen N. Growth mechanisms of high-shear pelletisation. International Journal of Pharmaceutics 1997;157(1):93 – 102. doi:10.1016/S0378-5173(97)00232-9.

39. Barrasso D, Ramachandran R. Qualitative assessment of a multi-scale, compartmental PBM-DEM model of a continuous twin-screw wet granulation process. Journal of Pharmaceutical Innovation 2016;11(3):231–49. doi:10.1007/s12247-015-9240-7.

40. Hapgood KP, Litster JD, Smith R. Nucleation regime map for liquid bound granules. AIChE Journal 2003;49(2):350–61.

41. Ennis BJ, Tardos G, Pfeffer R. A special volume devoted to the second symposium on advances in particulate technology a microlevel-based characterization of granulation phenomena. Powder Technology 1991;65(1):257 –72. doi:10.1016/0032-5910(91)80189-P.

42. Goodson M, Kraft M, Forrest S, Bridgwater J. A multi-dimensional population balance model for agglomeration. In: PARTEC 2004:International Congress for Particle Technology. 2004:.

43. Vercruysse J, Díaz DC, Peeters E, Fonteyne M, Delaet U, Assche IV, Beer TD, Remon J, Vervaet C. Continuous twin screw granulation: Influence of process variables on granule and tablet quality. European Journal of Pharmaceutics and Biopharmaceutics 2012;82(1):205 –11. doi:10.1016/j.ejpb.2012.05.010.

44. Lee KF, Patterson RIA, Wagner W, Kraft M. Stochastic weighted particle methods for population balance equations with coagulation, fragmentation and spatial inhomogeneity. Journal of Computational Physics 2015;303:1 – 18. doi:10.1016/j.jcp.2015.09.031.

45. Kumar A, Vercruysse J, Vanhoorne V, Toiviainen M, Panouillot PE, Juuti M, Vervaet C, Remon JP, Gernaey KV, Beer TD, Nopens I. Conceptual framework for model-based analysis of residence time distribution in twin-screw granulation. European Journal of Pharmaceutical Sciences 2015;71:25 – 34.

46. Allen T. Particle size measurement. Springer; 2013.

47. Sayin R. Mechanistic studies of twin screw granulation. PhD dissertation; Purdue University; 2016.

48. Hodgman CD. Handbook of chemistry and physics.; vol. 71. LWW; 1951.

49. Zadow JG. Lactose: Properties and uses. Journal of Dairy Science 1984;67(11):2654–79. doi:10.3168/jds.S0022-0302(84)81625-2.

50. Hooke R, Jeeves TA. "Direct search" solution of numerical and statistical problems. Journal of the ACM 1961;8(2):212–29. doi:10.1145/321062.321069.

51. Bratley P, Fox BL. Algorithm 659: Implementing Sobol's quasirandom sequence generator. ACM Transactions on Mathematical Software 1988;14(1):88–100. doi:10.1145/42288.214372.

52. MoDS . (Model Development Suite). Cambridge, United Kingdom: CMCL Innovations; 2015. https://cmclinnovations.com/products/mods/.

53. Dhenge RM, Fyles RS, Cartwright JJ, Doughty DG, Hounslow MJ, Salman AD. Twin screw wet granulation: Granule properties. Chemical Engineering Journal 2010;164(2-3):322 –9.

54. Fonteyne M, Fussell AL, Vercruysse J, Vervaet C, Remon JP, Strachan C, Rades T, Beer TD. Distribution of binder in granules produced by means of twin screw granulation. International Journal of Pharmaceutics 2014;462(1):8 – 10. doi:10.1016/j.ijpharm.2013.12.008.

55. Vercruysse J, Toiviainen M, Fonteyne M, Helkimo N, Ketolainen J, Juuti M, Delaet U, Assche IV, Remon JP, Vervaet C, Beer TD. Visualization and understanding of the granulation liquid mixing and distribution during continuous twin screw granulation using NIR chemical imaging. European Journal of Pharmaceutics and Biopharmaceutics 2014;86(3):383 –92. doi:10.1016/j.ejpb.2013.10.012.

56. Oullion M, Reynolds G, Hounslow M. Simulating the early stage of high-shear granulation using a two-dimensional Monte-Carlo approach. Chemical Engineering Science 2009;64(4):673 –85. doi:10.1016/j.ces.2008.08.014.

57. Thompson M, Sun J. Wet granulation in a twin-screw extruder: Implications of screw design. Journal of Pharmaceutical Sciences 2010;99(4):2090–103.

58. Kumar A, Vercruysse J, Bellandi G, Gernaey KV, Vervaet C, Remon JP, Beer TD, Nopens I. Experimental investigation of granule size and shape dynamics in twin-screw granulation. International Journal of Pharmaceutics 2014;475(1-2):485 –95. doi:10.1016/j.ijpharm.2014.09.020.

59. Lee KT, Ingram A, Rowson NA. Twin screw wet granulation: The study of a continuous twin screw granulator using positron emission particle tracking (PEPT) technique. European Journal of Pharmaceutics and Biopharmaceutics 2012;81(3):666 –73. doi:10.1016/j.ejpb.2012.04.011.

60. Eitzlmayr A, Koscher G, Reynolds G, Huang Z, Booth J, Shering P,

Khinast J. Mechanistic modeling of modular co-rotating twin-screw extruders. International Journal of Pharmaceutics 2014;474(1-2):157 –76. doi:10.1016/j.ijpharm.2014.08.005.

61. Djuric D, Kleinebudde P. Impact of screw elements on continuous granulation with a twin-screw extruder. Journal of Pharmaceutical Sciences 2008;97(11):4934–42. doi:10.1002/jps.21339.